Collimated propagation of fast electron beams accelerated by high-contrast laser pulses in highly-resistive shocked-carbon

X. Vaisseau, A. Morace, M. Touati, M. Nakatsutsumi, S. D. Baton, S. Hulin, Ph. Nicolai, R. Nuter, D. Batani, F. N Beg, et al.

Collimated propagation of fast electron beams accelerated by high-contrast laser pulses in highly-resistive shocked-carbon

X. Vaisseau,[1] A. Morace,[2] M. Touati,[1,3] M. Nakatsutsumi,[4] S. Baton,[4] S. Hulin,[1] Ph. Nicolaï,[1] R. Nuter,[1] D. Batani,[1] F.N. Beg,[5] J. Breil,[1] R. Fedosejevs,[6] J.-L. Feugeas,[1] P. Forestier-Colleoni,[1] C. Fourment,[1] S. Fujioka,[2] L. Giuffrida,[1] S. Kerr,[6] H.S. McLean,[7] H. Sawada,[8] V.T. Tikhonchuk,[1] and J.J. Santos[1,*]

[1] *Univ. Bordeaux, CNRS, CEA, CELIA (Centre Lasers Intenses et Applications), UMR 5107, F-33405 Talence, France*
[2] *Institute of Laser Engineering, Osaka University, 2-6 Yamadaoka, Suita, Osaka, Japan*
[3] *Department of Electrical Engineering, University of California Los Angeles, Los Angeles, CA 90095, USA*
[4] *LULI, Ecole Polytechnique CNRS/CEA/UPMC, 91128 Palaiseau Cedex, France*
[5] *University of California, San Diego, La Jolla, California 92093, USA*
[6] *Department of Electrical and Computer Engineering, University of Alberta, Edmonton T6G 2G7, Canada*
[7] *Lawrence Livermore National Laboratory, Livermore, California 94550, USA*
[8] *University of Nevada, Reno, Nevada 89557, USA*

(Dated: February 21, 2017)

Collimated transport of ultrahigh intensity electron current was observed in cold and in laser-shocked vitreous carbon, in agreement with simulation predictions. The fast electron beams were created by coupling high-intensity and high-contrast laser pulses onto copper-coated cones drilled into the carbon samples. The guiding mechanism – observed only for times before the shock breakout at the inner cone-tip – is due to self-generated resistive magnetic fields of $\sim 0.5-1$ kT arising from the intense currents of fast electrons in vitreous carbon, by virtue of its specific high-resistivity over the range of explored background temperatures. The spatial distribution of the electron beams, injected through the samples at different stages of compression, was characterized by side-on imaging of hard X-ray fluorescence.

PACS numbers:

The transport of intense currents of relativistic electron beams (REB) driven by intense lasers into dense matter is a key topic for applications such as secondary particle acceleration, x-ray and gamma-ray generation, isochoric heating to temperatures relevant in the context of planetology or astrophysics, and laser-driven thermonuclear fusion. The fast ignition scheme (FI) [1] proposes to ignite a pre-compressed capsule of deuterium-tritium fuel by the rapid energy-deposition from a REB. The key figure for FI-feasibility is the energy coupling of the ignitor laser pulse and the dense fuel-core: 20 kJ of 1-2 MeV electrons should be delivered into a 20 μm-radius hot spot [2]. The laser to REB energy-transfer can, in principle, be up to $\sim 40\%$ [3–6], yet the source angular distribution of REB momenta is intrinsically broad [7–9]. The use of a hollow cone re-entrant into the capsule provides a clear pathway for the ignitor laser till the cone tip [10, 11], moving the REB-source as close as 100 μm from the high-density core [12]. Yet, the challenge persists of confining the REB propagation within a small radius, while limiting both resistive and collisional energy losses over the compressed plasma [13–15] as well as REB-source perturbations either by cone-tip ablation by the laser intensity-pedestal [16–18] or by tip disruption due to the high-pressure of the asymmetrically imploded plasma [19].

No methods have been devised yet to control the REB divergence directly at the source, but a few strategies to magnetically collimate REB propagation have been proposed [20]. Magnetic-field (B-field) strengths in the range of kT, either self-generated or imposed, are needed to produce a sufficient effect on the MeV electrons. Self-generated B-fields arise from a resistive return current at high REB current densities, $j_h \gtrsim 10^{11}$ A.cm^{-2} [21]. Target structuring with different materials allows to obtain radially-convergent resistivity gradients. Such fields produced an observable collimation effect on REB-transport in both planar [22] and cylindrical [23] experimental designs. Numerical simulations explored the effect in even more complex cone-target structures [24–26]. However it is unlikely that they will survive the implosion and ignitor-laser irradiation. Other strategies explored experimentally are the REB interaction with radially-converging resistivity-gradients by cylindrical target-compression [27] or a precursor less-intense laser pulse generating a seed B-field [28]. Yet, in all the cases an efficient collimation, with small electron losses, has yet to be demonstrated.

Other studies pointed out that materials of higher atomic number, such as Au, of higher heat capacity and ionization level, yield higher resistivity-gradients over the REB time-scale, favoring its collimation through self-generated B-fields [29, 30]. Even though, such dense materials are prone to increase the collisional diffusion and energy losses of the beam electrons. A recent study pointed out that not so dense vitreous-carbon is highly resistive over a broader temperature range up to ~ 100 eV, therefore facilitating rapid B-field growth [31]

even under the conditions of very intense currents. Our experiment was focused on exploring REB transport in samples of such high-resistivity, while of relatively low-density, under conditions linked to the FI scenario: REB generated in cone targets and propagating into shock-compressed warm dense matter.

The experiment was carried out at the LULI2000 facility (Ecole Polytechnique, France). The targets consisted of a 10 μm-thick, 450 μm-long hollow Cu-cone buried in a 500 μm-thick vitreous-C layer of $\rho_0 = 2\,\mathrm{g.cm^{-3}}$-density [Fig. 1 a)]. A 10 μm Cu-tracer was located at a nominal distance $L_0 = 50\,\mu$m away from the outer cone tip, followed by a 15 μm plastic (CH) layer acting as an ablator. We used a dual laser beam setup: a compression shock was driven at the CH-side of the target by a frequency doubled long pulse (LP) laser ($\lambda_{LP} = 0.53\,\mu$m), with a $\tau_{LP} = 3$ ns square temporal profile ($\sim$ 100 ps rise-time). It was focused by means of a random phase plate onto a 340 μm flat-top spot containing $\sim$ 61% of the 496 ± 50 J on-target energy, yielding an intensity of $1.3 \times 10^{14}\,\mathrm{W.cm^{-2}}$. The $\lambda_{SP} = 1.053\,\mu$m, $\tau_{SP} = 1.3$ ps full-width-at-half-maximum (FWHM) short pulse (SP) laser was focused on the inner cone tip, of 50 μm diameter, in order to generate a REB propagating against the shock. A plasma mirror was used to direct the SP laser along the cone axis and to reduce its pedestal due to the amplified spontaneous emission (ASE) down to $\sim 10^{10}\,\mathrm{W.cm^{-2}}$ intensity. We obtained Gaussian-like focal spots of 10 μm FWHM containing $\sim$ 60% of the on-target 33 J SP-laser energy, yielding a peak intensity of $2 \times 10^{19}\,\mathrm{W.cm^{-2}}$. For each shot, the delay Δt between the two laser pulses (SP peak intensity in respect to the LP half-rise time), was set according to the required compression state of the target with a precision $\leq$ 50 ps. The chosen Δt were determined by a simulation of the shock formation and compression using the 2D radiative-hydrodynamic Lagrangian code CHIC [32], benchmarked by shock-breakout measurements on Al foils. The description of the shocked cone-targets' hydrodynamics was further benchmarked in a previous experiment by streaked optical pyrometry of the inner-cone tip and target side-on radiography using Cu K-shell ionization fluorescence as backlighter [33].

Fast electron generation and transport in the target were investigated from side-on imaging of the Cu-K$_\alpha$ ionization fluorescence from both the cone and the rear-side tracer using a spherically-bent Bragg crystal [34], providing simultaneous access to the REB spatial distribution at the source and after crossing the C-layer. Fig. 1 b) shows sample data as a function of Δt, from $\Delta t = 0$ ns (REB injection into an unperturbed solid-cold vitreous-C target), up to $\Delta t = 4$ ns (1 ns after shock-breakout time at the inner cone-tip surface; REB generation in an expanding plasma filling the cone volume). The use of the LP laser also for the $\Delta t = 0$ -case allowed the formation of a long CH ablation-plasma that prevented fast electrons from recirculating after their first transit through the Cu layers [13, 35]. The simulated density and temperature maps at the corresponding delays are presented on Fig. 1 c). At $\Delta t = 3$ ns, just before shock breakout, the C-layer density is increased by a factor ~ 2.7 over its full thickness while its temperature reaches ~ 3 eV. Looking only at the cone emission for times before shock-breakout, it mainly originates from the tip, highlighting the efficiently localized energy coupling of the high-contrast SP laser.

The emission from the rear side tracer is also clearly visible for the two earlier times, showing that a significant fraction of the REB energy was transported into the target depth. For $\Delta t = 2.5$ ns, the rear side tracer is being pushed towards the cone tip by the compression shock, as seen on the hydro simulation. The tracer fluorescence yield is higher with respect to the $\Delta t = 0$ image, in relation to a reduction of the fast electrons energy-loss due to the resistive effect (collisional losses are kept the same for samples of identical areal mass) [13]. An important feature is that the tracer emission size is of the same order as that from the cone tip, consistent with its 50 μm-diameter, despite the several tens of microns propagation distances, as it is shown on Fig. 2 a) by the measured diameters of the tracer-fluorescence (blue full triangles). This data set demonstrates a collimated propagation of the REB over the carbon layer, either entirely cold-solid ($\Delta t = 0$ ns), or partially ($\Delta t = 1$ ns, $\Delta t = 2$ ns) or entirely in warm-dense state ($\Delta t = 2.5$ ns, when the shock front is entering the cone tip). Such collimation was confirmed by doubling the cone tip-Cu tracer distance to $L_0 = 100\,\mu$m, resulting in a Cu-K$_\alpha$ diameter of $\sim 60\,\mu$m for the unperturbed target [blue full square on Fig. 2 a)]. Given the longer propagation distance, this is still fairly close to the cone-tip diameter. For $\Delta t \geq 3$ ns the emission from the Cu tracer can no longer be distinguished from the emission of the cone tip as the distance between them, as predicted by the hydro simulation and target radiography results [33], is smaller than the $\sim 10\,\mu$m-resolution of the Cu-K_α imager. The tip fluorescence yield reaches its highest value at $\Delta t = 3$ ns due to the peak Cu-density under the shock.

The fluorescence patterns are significantly different when injecting fast electrons after the shock breakout inside the cone ($\Delta t > 3$ ns). Fast electrons were then generated in an expanding Cu plasma progressively filling the volume of the cone. As evidenced from the image at $\Delta t = 4$ ns (note the different spatial scale), this dramatically increased electron divergence, their dilution into the plasma-filled cone volume and the length of their interaction with the cone walls. Consistently, the Cu-K_α yield decreases. A steep decrease in the global energy coupling to the target depth after shock breakout is corroborated from spatially integrated measurements of the Cu-K_α yield as a function of the delay between the two laser pulses, using a potassium acid phthalate (KAP) conical crystal at the 5th diffraction order (not

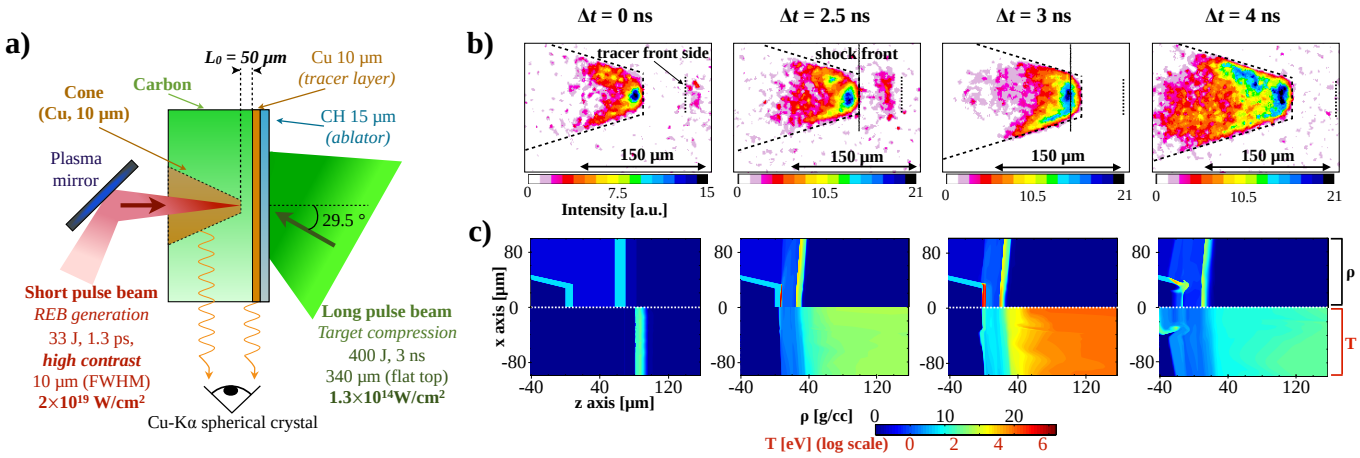

FIG. 1. (color online) **a)** Experimental setup: target design, geometry of laser irradiation and Cu-K$_\alpha$ sight axis (top view). **b)** Experimental side-on images of the Cu-K$_\alpha$ fluorescence, attributable to the time-integrated REB spatial distributions, as a function of Δt. Note the different signal-intensity scales. Dashed lines indicate the initial position of the cone walls and the front surface of the Cu tracer. The dotted lines indicate the shock-front positions. **c)** Density (top) and temperature (bottom) maps as a function of the delay between the laser pulses Δt, obtained with 2D rad-hydro simulations. The maps' aspect ratio has been modified for clarity.

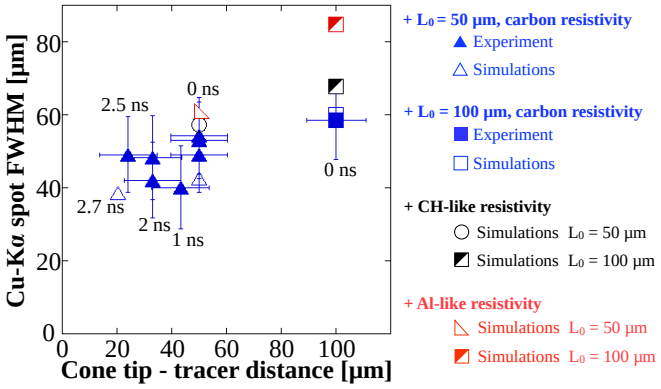

FIG. 2. (color online) Evolution of the rear-side tracer Cu-K_α spot diameter as a function of the distance between the tracer layer and the cone tip for two different initial (un-driven) distances, $L_0 = 50\,\mu$m (blue full triangles) and $L_0 = 100\,\mu$m (blue full square) targets. REB-transport simulation results are shown for comparison (blue open symbols). Simulated results obtained by using the CH-like (black open disk and black half-filled square, corresponding to $L_0 = 50\,\mu$m and $L_0 = 100\,\mu$m, respectively) and Al-like (red semi-square and red half-filled square, corresponding to $L_0 = 50\,\mu$m and $L_0 = 100\,\mu$m, respectively) resistivities are also shown. The corresponding time delays between the laser pulses are given for each abscissa, as an indication of the different compression states of the C-layer.

presented) [36].

To further understand the physics at play, in particular the mechanisms of REB collimation/dispersion, the experimental data were compared to a suite of numerical simulations. The REB source was computed with the 1D particle-in-cell (PIC) code OCEAN [37] modeling the interaction between the SP beam and the Cu generation layer. Collisions were not taken into account since the goal of these PIC simulations was only to estimate the energy spectra of the REB source. The SP temporal profile was a 1.5 ps FWHM Gaussian with a peak intensity of 10^{19} W.cm^{-2}. We considered four different compression delays corresponding to those shown on Fig. 1, the $\Delta t = 0$ and 2.5 ns cases corresponding to an uncompressed cone tip. In the cases before shock breakout time the pre-plasma gradient length was set to 0.2 μm, due to the high-contrast of the laser pulse. The REB source characteristics were extracted after crossing the same quantity of matter in each simulation (same 4.5 mg.cm^{-2} areal mass), corresponding to a 5 μm depth into the cone Cu layer for the unperturbed cone-tip cases. The REB-source energy distributions, averaged over the 5.3 ps-duration of the simulations, are presented in Fig. 3 a). Since the distributions are fairly similar before shock breakout time, only two cases are shown in the figure. The REB distribution exhibits a 1.5 MeV temperature component when generated on a several microns length plasma ramp (after shock breakout time), which is not present for interactions at the early times. The REB mean energy rises from $\sim$ 20 keV to $\sim$ 170 keV before and after shock breakout time, respectively. The predicted total number of accelerated electrons is higher in the last case by virtue of a higher laser energy absorption over the long scale-length plasma, yet the energy coupling into the dense target regions is reduced due to the fast electrons dilution into the plasma ramp and cone walls, as inferred from the Cu-K$_\alpha$ images described above.

The REB transport was simulated with a reduced ki-

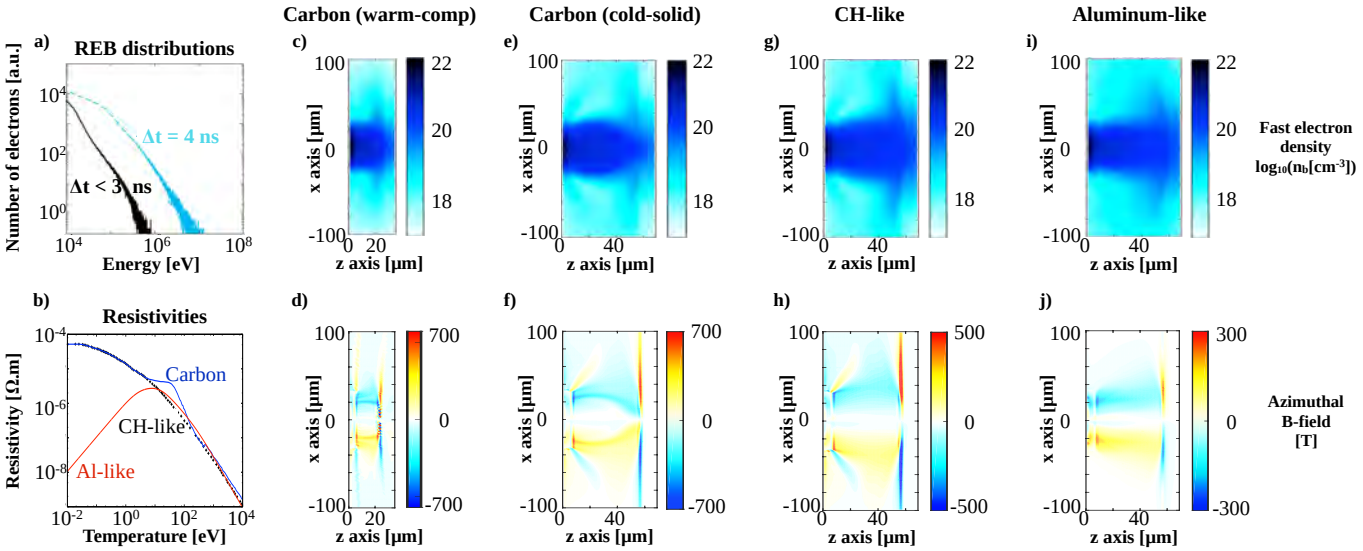

FIG. 3. (color online) **a)** Fast electron source energy distribution extracted from PIC simulations before shock breakout time (black solid line) and 1 ns after shock breakout time (blue dashed line). **b)** Electric resistivity functions used in transport simulations: nominal resistivity of vitreous-C, from [42] (blue solid line), CH-like resistivity obtained by suppressing the *bump* in the $6-70$ eV range (black dotted line) and Al resistivity (red solid line). On the top, **c)**, **e)**, **g)** and **i)**: fast electron density maps extracted from transport simulations at 2.7 ps, the time of the peak azimuthal B-field [maps on the bottom, **d)**, **f)**, **h)** and **j)**; note the different color scales]. Simulations with vitreous-C resistivity: **c)** and **d)** $L_0 = 50\,\mu$m-case just before shock breakout time ($\Delta t = 3$ ns, the C-layer is fully compressed), **e)** and **f)** un-driven $L_0 = 50\,\mu$m-case. **g)** and **h)** Un-driven $L_0 = 50\,\mu$m-case using the CH-like resistivity. **i)** and **j)** Un-driven $L_0 = 50\,\mu$m-case using the Al resistivity. The $z = 0$-coordinate corresponds to the inner cone-tip surface.

netic code solving the linearized Vlasov-Fokker-Planck equation with an M1 approximation [38]. The 2D hydro simulation results, described above, were used as initial density and temperature profiles at the corresponding REB injection times. The SP laser energy was 33 J and laser-to-fast electron conversion efficiency $\eta_{L\to e} = 20\%$ before shock breakout time (in agreement with Davies' scaling law [39]). The fast electron angular distribution was described by a mean propagation angle $\theta_0 \sim 25° \tanh[r/r_b]$, with r the transverse coordinate and $r_b = 8.5\,\mu$m, and a mean dispersion angle $\Delta\theta = 25°$, in agreement with Green's scaling law [8]. Transport simulations were ran up to 4 ns with space and energy grids of 1 μm and 10 keV, respectively. Carbon resistivity at solid-density was inferred from quantum molecular dynamics calculations [42] and extended to high temperatures $\gtrsim$ 500 eV using the Spitzer model [43] [Fig. 3 b) (blue solid line)]. As the compression was relatively small, the same expressions were used for the resistivity of shocked carbon. The Cu and Al resistivities were calculated with the Drude model, $\eta = m_e\nu/e^2 n_e$, with n_e the electron density and ν the collision frequency given by a harmonic mean between the Lee & More model [40] for hot plasma temperatures and the Eidmann-Chimier model [41] for lower solid-liquid temperatures. The Cu-K_α emission was characterized using a model based on the Hombourger's cross sections [44] and the computation model proposed in [45]. The careful description of the REB source, the target hydrodynamics and the transient resistivity evolution resulted in a good agreement between the size of the synthetic [blue empty symbols in Fig. 2 a)] and the measured Cu-K_α spots at the different positions of the rear side Cu-tracer. This confirms the collimation of fast electrons in both compressed (warm and dense) [Fig. 3 c), $L_0 = 50\,\mu$m-case at $\Delta t = 3$ ns] and cold-solid carbon layers [Fig. 3 e), un-driven $L_0 = 50\,\mu$m-case]. This behavior can be explained by looking at the corresponding maps of azimuthal self-generated B-field [Fig. 3 d) and f)]. The collimating field of $\gtrsim 500$ T seen in the high-resistivity C-layer mainly originates from the curl of the REB current density, largely compensating the decollimating effect due to resistivity gradients arising from the rapid REB energy deposition along the cone axis.

In order to confirm the crucial role played by the vitreous-C resistivity, we performed two additional simulation tests consisting i) in suppressing the *bump* seen at $\sim 6-70$ eV temperature range in the vitreous-C resistivity [black dotted line on Fig. 3 b), labeled CH-like], and ii) in using instead the resistivity of Al (a conductive material) [red solid line on Fig. 3 b)]. The suppression of the C resistivity *bump* alone (first test) already reduces by a factor of 2 the amplitude of the self-generated B-field, yielding a much less collimated REB propagation [Fig. 3

g) and h)]. In the second test, the B-field is even weaker and the REB is significantly divergent [Fig. 3 i) and j)]. These two tests yield synthetic Cu-K_α spot sizes [respectively the black open circle and the red semi-square for $L_0 = 50\,\mu$m, and the black and red half-filled squares for $L_0 = 100\,\mu$m in Fig. 2 a)], larger than those obtained for vitreous-C in both experiments and simulations.

The enhancement of the REB energy density flux associated with the collimated transport in vitreous-C compared to other materials is however mitigated by an increase of the resistive energy losses due to the vitreous-C higher resistivity: These increase by $\sim 25\%$ over $50\,\mu$m of C when compared to the less resistive Al case. It is nonetheless worth to point out that the additional number of electrons stopped in vitreous-C consists of the less energetic component of the REB spectrum, which would in any case be stopped before reaching the compressed DT-core in a FI fusion target.

In all cases is possible to identify an enhanced radial diffusion of the lower-energy electrons when reaching the Cu-tracer (denser than the C layers) as well as the development of surface B-fields at the C-Cu interfaces attributable to the corresponding resistivity discontinuities. Yet, these features do not interfere with the conclusions concerning the role of resistivity in the electron transport through the C-layers (shocked or undriven) and from the comparison of transport in C, CH or Al.

In conclusion, we characterized the spatial distribution of relativistic electron beams generated by coupling a high-intensity laser pulse into a vitreous carbon target in both cold-solid and warm-dense conditions. The use of a high-contrast laser pulse allowed its efficient coupling to the tip of a cone drilled into the target before shock breakout time. A strong dilution of the fast electron source was observed when firing the laser pulse after shock breakout, confirming the deleterious effect on the REB energy-density flux due to plasma-filling of the cone [16–19]. More importantly, a clear collimation of the fast electron beam over several tens of microns distances was experimentally achieved in both cold-solid and warm-dense vitreous C propagation layers, and reproduced by numerical transport simulations. This remarkable behavior is attributed to the high-resistivity of vitreous C, generating several hundreds of Teslas collimating B-fields, even under compressed matter conditions and over a wide range of temperatures up to 100 eV. An additional set of transport simulations using different materials confirmed the importance of the C high resistivity in this range of temperatures. As a counterpart, the high resistivity of vitreous-C was responsible for additional resistive energy losses when compared to the less resistive cases. Noteworthily, the collisional losses are kept low by virtue of the C low-density, an advantage compared to other studies proposing high-resistivity propagation media using high-Z materials of larger heat capacity and higher ionization level [29, 30]. The explored behavior of vitreous-C can be of considerable importance for an advanced design of a FI target by inserting a low-density and high-resistivity plug to a (thinner, $\sim \mu$m) cone-tip of a denser material: The light and resistive plug, placed close to the REB source, would be thick enough to mitigate the REB natural divergence, but thin enough to moderate the subsequent rise of resistive energy losses.

We gratefully acknowledge the support of the LULI pico 2000 staff during the experimental run. This work was performed through the funding from the French National Agency for Research (ANR) and the Competitiveness Cluster Alpha - Route des Lasers, Project TERRE ANR-2011-BS04-014. The work was carried out in the framework of the Investments for the future Programme IdEx Bordeaux LAPHIA (ANR-10-IDEX-03-02) and the EUROfusion Consortium, and has received funding from the European Union's Horizon 2020 research and innovation program under Grant No. 633053. The views and opinions expressed herein do not necessarily reflect those of the European Commission.

* joao.santos@u-bordeaux.fr

[1] M. Tabak, J. Hammer, M.E. Glinsky, W.L. Kruer, S.C. Wilks, J. Woodworth, E.M. Campbell, M.D. Perry, R.J. Mason, Phys. Plasmas **1**, 1626 (1994).
[2] S. Atzeni, A. Schiavi and J.R. Davies Plasma Phys. Control. Fusion **51**, 1, 015016 (2009).
[3] K.B. Wharton, S. Hatchett, S.C. Wilks et al. Phys. Rev. Lett. **81**, 4, 822–825 (1998).
[4] P.M. Nilson, A.A. Solodov, J.F. Myatt et al. Phys. Rev. Lett. **105**, 23, 235001 (2010).
[5] B. Westover, C.D. Chen, P.K. Patel et al. Phys. Plasmas **18**, 6, 063101 (2011).
[6] B. Westover, C.D. Chen, P.K. Patel et al. Phys. Plasmas **21**, 3, 031212 (2014).
[7] J.C. Adam, A. Héron, G. Laval, Phys. Rev. Lett. **97**, 205006 (2006).
[8] J.S. Green, V.M. Ovchinnikov, R.G. Evans et al., Phys. Rev. Lett. **100**, 015003 (2008).
[9] A. Debayle, J.J. Honrubia, E. d'Humières, V.T. Tikhonchuk, Phys. Rev. E **82**, 036405 (2010).
[10] P.A. Norreys, R. Allot, R.J. Clarke et al., Phys. Plasmas **7**, 3721 (2000).
[11] R. Kodama, H. Shiraga, K. Shigemori, et al., Nature **418**, 933–934 (2002).
[12] H.D. Shay, P. Amendt, D. Clark, D. Ho et al. Phys. Plasmas **19**, 9, 092706 (2012).
[13] X. Vaisseau, A. Debayle, J.J. Honrubia et al., Phys. Rev. Lett. **114**, 095004 (2015).
[14] J.J. Santos, A. Debayle, Ph. Nicolaï, V. Tikhonchuk, et al. Phys. Plasmas **14**, 10, 103107 (2007).
[15] B. Vauzour, A. Debayle, X. Vaisseau, S. Hulin, et al. Phys. Plasmas **21**, 3, 033101 (2014)
[16] S. Baton, M. Koenig, J. Fuchs et al., Phys. Plasmas **15**, 042706 (2008).
[17] A.G. MacPhee, L. Divol, A. Kemp et al., Phys. Rev. Lett.

104, 055002 (2010).
[18] T. Ma, H. Sawada, P.K. Patel et al., Phys. Rev. Lett. **108**, 115004 (2012).
[19] W. Theobald, A.A. Solodov, C. Stoeckl et al., Phys. Plasmas **18**, 3721 (2011).
[20] A.P.L. Robinson, D.J. Strozzi, J.R. Davies, L. Gremillet, J.J. Honrubia, T. Johzaki, R.J. Kingham, M. Sherlock, A.A. Solodov Nucl. Fusion **54** 054003 (2014).
[21] A.R. Bell and R.J. Kingham, Phys. Rev. Lett. **91**, 035003 (2003).
[22] S. Kar, A.P.L. Robinson, D.C. Carroll, O. Lundh, K. Markey, P. McKenna, P. Norreys, M. Zepf, Phys. Rev. Lett. **102**, 055001 (2009).
[23] B. Ramakrishna, S. Kar, A.P.L. Robinson et al., Phys. Rev. Letters **105**, 135001 (2010).
[24] A.P.L. Robinson, M.H. Key, M. Tabak, Phys. Rev. Lett. **108**, 125004 (2012).
[25] H. Schmitz, R. Lloyd, R.E. Evans Plasma Phys. Control. Fusion **54**, 085016 (2012).
[26] A. Debayle, L. Gremillet, J.J. Honrubia, E. d'Humières Phys. Plasmas **20**, 013109 (2013).
[27] F. Pérez, A. Debayle, J. Honrubia et al., Phys. Rev. Lett. **107**, 065004 (2011).
[28] R.H.H. Scott, C. Beaucourt, H.-P. Schlenvoigt et al., Phys. Rev. Lett. **109**, 015001 (2012).
[29] Y. Sentoku, E. d'Humières, L. Romagnani, P. Audebert and J. Fuchs Phys. Rev. Lett. **107**, 135005 (2011).
[30] S. Chawla, M.S. Wei, R. Mishra et al. Phys. Rev. Lett. **110**, 025001 (2013).
[31] D.A. MacLellan, D.C. Carroll, R.J. Gray et al., Phys. Rev. Lett. **111**, 095001 (2013).
[32] P.-H Maire, R. Abgrall, J. Breil, and J. Ovadia, SIAM. J. Sci. Comput. **29**, 1781 (2007).
[33] A. Morace, L. Fedeli, D. Batani et al., Phys. Plasmas **21**, 102712 (2014).
[34] R.B. Stephens, R.A. Snavely, Y. Aglitskiy et al., Phys. Rev. E **69**, 066414 (2004).
[35] B. Vauzour, J.J. Santos, A. Debayle et al., Phys. Rev. Lett. **109**, 255002 (2012).
[36] E. Martinolli, M. Koenig, J.M. Boudenne, E. Perelli, D. Batani and T.A. Hall, Rev. Sci. Instrum. **75**, 2024 (2004).
[37] R. Nuter, and V.T. Tikhonchuk, Phys. Rev. E **87**, 043109 (2013).
[38] M. Touati, J-L Feugeas, Ph. Nicolaï, J.J. Santos, L. Gremillet and V.T. Tikhonchuk New. J. Phys. **16**, 073014 (2014).
[39] J.R. Davies, Plasm. Phys. and Control. Fusion **51**, 014006 (2009).
[40] Y.T. Lee and R.M. More, Phys. Fluids **27**, 1273 (1984).
[41] B. Chimier, V.T. Tikhonchuk and L. Hallo Phys. Rev. B **75**, 195124 (2007).
[42] P. McKenna, A.P.L Robinson, D. Neely et al., Phys. Rev. Lett. **106**, 185004 (2011).
[43] L. Spitzer, and R. Härm, Phys. Rev. **89**, 977 (1953).
[44] C. Hombourger, J. Phys. B **31**, 3693 (1998).
[45] A.G.R. Thomas, M. Sherlock, C. Kuranz, C.P. Ridgers and R.P. Drake, New. J. Phys. **15**, 015017 (2013).